THE JOURNAL OF BIOLOGICAL CHEMISTRY VOL. 289, NO. 29, pp. 20259–20272, July 18, 2014

Structural Basis of G Protein-coupled Receptor-G_i Protein Interaction

*FORMATION OF THE CANNABINOID CB_2 RECEPTOR-G_i PROTEIN COMPLEX**

Received for publication, December 9, 2013, and in revised form, May 18, 2014 Published, JBC Papers in Press, May 22, 2014, DOI 10.1074/jbc.M113.539916

Jagjeet S. Mnpotra[‡], Zhuanhong Qiao[§], Jian Cai[§], Diane L. Lynch[‡], Alan Grossfield[¶], Nicholas Leioatts[¶], Dow P. Hurst[‡], Michael C. Pitman[‡‖], Zhao-Hui Song[§1], and Patricia H. Reggio[‡2]

From the [‡]Department of Chemistry and Biochemistry, University of North Carolina, Greensboro, North Carolina 27402, the [§]Department of Pharmacology and Toxicology, University of Louisville School of Medicine, Louisville, Kentucky 40292, the [¶]Department of Biochemistry and Biophysics, University of Rochester Medical Center, Rochester, New York 14642, and the [‖]Computational Biology Center, IBM Thomas J. Watson Research Center, Yorktown Heights, New York 10598

Background: CB_2 couples with only G_i protein.
Results: Cross-linking studies using LC-MS/MS and ESI-MS/MS identified three specific CB_2-Gα_i cross-link sites. MD showed an orientation change from the β2-AR*/G_s geometry makes all cross-links possible.
Conclusion: Second intracellular loop of CB_2 interactions are key for G_i complex formation.
Significance: Findings should be relevant for other GPCRs that couple to G_i proteins.

In this study, we applied a comprehensive G protein-coupled receptor-Gα_i protein chemical cross-linking strategy to map the cannabinoid receptor subtype 2 (CB_2)- Gα_i interface and then used molecular dynamics simulations to explore the dynamics of complex formation. Three cross-link sites were identified using LC-MS/MS and electrospray ionization-MS/MS as follows: 1) a sulfhydryl cross-link between C3.53(134) in TMH3 and the Gα_i C-terminal i-3 residue Cys-351; 2) a lysine cross-link between K6.35(245) in TMH6 and the Gα_i C-terminal i-5 residue, Lys-349; and 3) a lysine cross-link between K5.64(215) in TMH5 and the Gα_i $\alpha_4\beta_6$ loop residue, Lys-317. To investigate the dynamics and nature of the conformational changes involved in CB_2·G_i complex formation, we carried out microsecond-time scale molecular dynamics simulations of the CB_2 R*·G$\alpha_{i1}\beta_1\gamma_2$ complex embedded in a 1-palmitoyl-2-oleoyl-phosphatidylcholine bilayer, using cross-linking information as validation. Our results show that although molecular dynamics simulations started with the G protein orientation in the β2-AR*·G$\alpha_s\beta_1\gamma_2$ complex crystal structure, the G$\alpha_{i1}\beta_1\gamma_2$ protein reoriented itself within 300 ns. Two major changes occurred as follows. 1) The Gα_{i1} α5 helix tilt changed due to the outward movement of TMH5 in CB_2 R*. 2) A 25° clockwise rotation of G$\alpha_{i1}\beta_1\gamma_2$ underneath CB_2 R* occurred, with rotation ceasing when Pro-139 (IC-2 loop) anchors in a hydrophobic pocket on Gα_{i1} (Val-34, Leu-194, Phe-196, Phe-336, Thr-340, Ile-343, and Ile-344). In this complex, all three experimentally identified cross-links can occur. These findings should be relevant for other class A G protein-coupled receptors that couple to G_i proteins.

G protein-coupled receptors (GPCRs)[3] represent excellent drug targets because they are involved in regulating nearly all known physiological functions (1, 2). Class A GPCRs are thought to have a common topology that includes an extracellular N terminus, a transmembrane core formed by a bundle of seven transmembrane α-helices (TMH1–7), three extracellular (EC) and three intracellular (IC) loops that connect these helices, and an intracellular C terminus that begins with a short amphipathic helix lying parallel to the membrane (3–6). Physiologically, GPCRs are activated by ligands (extracellular and membrane-based) that enable the receptors to interact with and activate distinct sets of heterotrimeric G proteins (G$\alpha\beta\gamma$), as well as β-arrestins (7, 8). Specifically, ligand-activated GPCRs catalyze the exchange of GDP for GTP on the Gα subunit. GTP binding to Gα is predicted to trigger the dissociation of the heterotrimeric G protein into Gα-GTP and free $\beta\gamma$, which are then able to modulate the activity of a multitude of downstream effectors, including adenylate cyclase and ion channels, such as G protein-gated inwardly rectifying potassium channels (GIRK2 and GIRK4), phospholipase Cβ, and plasma membrane Ca^{2+} pumps (9–12).

The CB_2 receptor belongs to class A of the GPCRs and is mainly expressed in T cells of the immune system (13) and the gastrointestinal system (14, 15). CB_2 has also been reported to play an important role in central immune responses during neuropathic pain in mice (16). We have previously performed microseconds long MD simulations of the CB_2 endogenous ligand, *sn*-2-arachidonoylglycerol (2-AG), entering and activating CB_2 via the lipid bilayer (17). Activation of CB_2 has been shown experimentally to produce coupling to Gα_i inhibitory protein (18–20). Although a significant amount of information

* This work was supported, in whole or in part, by National Institutes of Health Grants DA011551 (to Z. H. S.), GM095496 (to A. M. G.), and DA003934 and DA021358 (to P. H. R.).
[1] To whom correspondence may be addressed. E-mail: zhsong@louisville.edu.
[2] To whom correspondence may be addressed: Dept. of Chemistry and Biochemistry, University of North Carolina, Patricia A. Sullivan Science Bldg., P. O. Box 26170, Greensboro, NC 27402-6170. Tel.: 336-334-5333; Fax: 336-334-5402; E-mail: phreggio@uncg.edu.

[3] The abbreviations used are: GPCR, G protein-coupled receptor; CB_2, cannabinoid receptor Sub-type 2; R*, activated receptor; POPC, 1-palmitoyl-2-oleoyl-phosphatidylcholine; β2-AR, β2-adrenergic receptor; MD, molecular dynamics; IC, intracellular; TMH, transmembrane helix; DSS, disuccinimidyl suberate; MS, mass spectrometry; VdW, van der Waals; Hx8, helix 8; ESI, electrospray ionization; r.m.s.d., root mean square deviation; GTPγS, guanosine 5′-3-*O*-(thio)triphosphate.

is available for GPCR-catalyzed activation of G proteins (21), many atomic level details concerning complex formation and signal transduction remain unanswered.

In this work, we studied the formation of a CB_2R^*·G protein complex both experimentally and computationally. Systematic cross-linking experiments were performed using $HgCl_2$ and a short bi-functional, irreversible chemical cross-linker disuccinimidyl suberate (DSS). These studies yielded three specific contact sites between CB_2 and $G\alpha_{i1}$ protein, providing new insights into the molecular architecture of the CB_2 and $G\alpha_{i1}$ interaction. Then, to place these cross-links in a structural perspective and also to explore the dynamic formation of the CB_2R^*·$G\alpha_{i1}\beta_1\gamma_2$ complex, we undertook two independent microsecond-long molecular dynamics simulations of the CB_2R^*·$G\alpha_{i1}\beta_1\gamma_2$ complex in a POPC bilayer. These studies revealed a stepwise formation of the complex that brings all cross-linked pairs into spatial proximity.

MATERIALS AND METHODS

Cell Transfection and Culture

Human embryonic kidney 293 (HEK293) cells were maintained in Dulbecco's modified Eagle's medium (DMEM) containing 10% fetal bovine serum, 2 mM glutamine, 100 units/ml penicillin, and 100 μg/ml streptomycin in a humidified atmosphere consisting of 5% CO_2 at 37 °C. Expression plasmids containing the N-terminal FLAG peptide (DYKDDDDK)-tagged human CB_2 cannabinoid receptors were stably transfected into HEK293 cells using Lipofectamine, according to manufacturer's instructions. Stably transfected cells were selected in culture medium containing 800 μg/ml geneticin. Having established cell lines stably expressing FLAG-CB_2 receptors, the cells were maintained in growth medium containing 400 μg/ml geneticin until needed for experiments.

Cross-linking Reactions and Purification of the Cross-linked Protein Complex

The CB_2 receptor has been shown to exhibit high constitutive activity (19). For this reason, cross-linking experiments were conducted in the absence of exogenous agonist. For each cross-linker, the cross-linking reactions were performed according to the manufacturer's instructions. Briefly, cells expressing FLAG-CB_2 receptors were collected, and cell membranes were prepared as described previously (22) in 20 mM HEPES buffer containing 150 mM NaCl. After adding cross-linkers at a final concentration of 2 mM, the cell membranes were incubated on ice for 2 h. At the end of incubation, the cross-linking reactions were terminated by adding quench solutions. Subsequently, Triton X-100 was added to a final concentration of 1%, and the membrane suspension was incubated at 4 °C for 2 h by end-to-end gentle rotations. The suspension was then centrifuged at 100,000 × *g* for 1 h at 4 °C to remove unsolubilized particles. For anti-FLAG M2 affinity chromatography, the solubilized suspension was incubated with 0.5 ml of anti-FLAG M2-agarose affinity gel at 4 °C for 2 h with gentle rocking. After extensive washing with 20 mM HEPES containing 150 mM NaCl and 1% Triton X-100, the bound CB_2 was eluted with 8-column volumes of 0.1 mM glycine HCl, pH 2.5, containing 1% Triton X-100.

In-gel Digestion

The purified CB_2 complex was resolved by SDS-PAGE and then subjected to Western blot and Coomassie Blue staining. Both anti-CB_2 antibody and anti-G protein antibody were used to identify the band corresponding to the CB_2·G protein complex. The CB_2·G protein complex band was then excised from Coomassie Blue-stained gel and subjected to enzymatic digestions according to a published protocol (22, 23) with slight modifications. Briefly, the bands were cut into small pieces, destained with 50 mM NH_4HCO_3/acetonitrile (1:1, v/v), and digested with 10 ng/μl pepsin overnight.

ESI-MS/MS

Peptides from the enzymatic digests were analyzed by ESI-MS/MS as described previously (22). Briefly, peptides from the enzymatic digests were condensed to 1–2 μl with a Speedvac, diluted with 5 μl of 0.2% trifluoroacetic acid (TFA), and analyzed by a Waters CapLC coupled to a Q-TOF API-US mass spectrometer (Waters, Milford, MA). The samples (5 μl) were injected onto a 300-μm × 5-mm PepMap C18 precolumn (LC Packing, Sunnyvale, CA), washed with 5% ACN in 0.1% formic acid at 30 μl/min for 3 min, eluted onto and separated with a 75-μm × 150-mm Atlantis dC18 analytical column (Waters). Separation was started with a 5-min isocratic elution with 95% solvent A (5% ACN with 0.1% formic acid) and 5% solvent B (95% ACN with 0.1% formic acid) and followed by a linear gradient from 5% solvent B to 40% solvent B over 115 min and then from 40% solvent B to 60% solvent B in 30 min. The flow rate on the column was about 200 nl/min. The eluted peptides were directed to a Q-TOF API-US mass spectrometer with a nanoflow source, and MS and MS/MS spectra were acquired by data-dependent scan.

Data analyses were performed with the aid of on-line server MS3D (24, 25). First, the precursor peptide ions from LC-MS/MS were screened by the "Links" program from MS3D. Links calculates the theoretical cross-linking possibilities for the CB_2·G protein complex, with information provided about the cross-linkers and protease used and the expected amino acid modifications. The Links program then gives us putative assignments within a defined mass error threshold for a list of input mass (MH^+) values. Once the candidates of CB_2-G protein cross-linked peptides were obtained, each candidate peptide was further analyzed by the "MS2Links" program from MS3D. MS2Links is a program for assigning tandem MS peak lists generated from the fragmentation of cross-linked, modified, or unmodified peptides. MS2Links calculate the theoretical MS/MS fragment library given information about the identity of the base ion, cross-linkers, desired ion types, and amino acid modifications. MS2Links then returns assignments within a defined mass error threshold for the list of input mass (MH^+) values.

Molecular Modeling

CB_2 Receptor Model—The CB_2 model employed here was taken from our previous microsecond-long simulation of the activation of the CB_2 receptor by the endogenous ligand, 2-AG, via the lipid bilayer (17). In this simulation, the ionic lock at the IC ends of TMH3-TMH6 (R3.55–D6.30) was broken within 3 ns of a 2-AG headgroup entry between TMH6 and TMH7 from the lipid bilayer (POPC). To represent the CB2-activated state,

we chose coordinates corresponding to time point 184.138 ns from trajectory E in which the salt bridge between TMH3 and TMH6 is broken (17). The α-carbon distance between R3.55(136) and D6.30(240) was 15.2 Å, and the heteroatom distance N (R3.55(136))-O (D6.30(240)) was 12.7 Å (17). In this bundle, the C terminus contains the palmitoylation site at Cys-320 and was truncated after Gly-322.

G Protein Modeling—For this study, the crystal structure of $G\alpha_{i1}\beta_1\gamma_2$ (26) was used to dock with CB_2 R*. The extreme $G\alpha_{i1}$ C terminus is unresolved in this structure, so the undecapeptide NMR structure (27) of this region in $G\alpha_t$ was grafted onto the backbone of residues Lys-345, Asn-346, and Asn-347 (see "Discussion"). The C terminus of $G\gamma_2$ is also unresolved in the $G\alpha_{i1}\beta_1\gamma_2$ structure. This region was built by homology modeling using the NMR structure of $G\gamma_1$ (28) as template and the Maestro module from Schrodinger, LLC, New York.

Lipidation Sites—Palmitic acid was attached to the N terminus of $G\alpha_{i1}$ at Cys-3 (29). Myristic acid was attached to Gly-2 of $G\alpha_{i1}$ (30), and a geranylgeranyl group was attached to Cys-68 in the $G\gamma_2$ C terminus (31).

CB_2·G_i Protein Complex—The relative orientations of CB_2 R* and $G\alpha_{i1}\beta_1\gamma_2$ were based on the β2-AR·$G\alpha_s\beta_1\gamma_2$ complex crystal structure (32). To get a relative receptor position, first the activated CB_2 receptor was superimposed onto the α carbon atoms of the residues N1.50, D2.50, R3.50, and W4.50 on the β2-AR receptor from the β2-AR·$G\alpha_s\beta_1\gamma_2$ complex. To obtain the relative orientation of $G\alpha_{i1}\beta_1\gamma_2$ heterotrimer with the CB_2 receptor, $G\beta_1$ of $G\alpha_{i1}\beta_1\gamma_2$ was superimposed on the α carbon atoms of residues from 51 to 340 of $G\beta_1$ in the $G\alpha_s\beta_1\gamma_2$ protein from the β2-AR·$G\alpha_s\beta_1\gamma_2$ complex. To relieve steric clashes between CB_2 and $G\alpha_{i1}$, the whole $G\alpha_{i1}\beta_1\gamma_2$ heterotrimer was translated in the z-direction.

Construction of CB_2·$\alpha_{i1}\beta_1\gamma_2$ Complex in POPC Bilayer

The CB_2 R*·G protein complex was aligned such that the transmembrane region of the CB_2 receptor was centered at the middle of the POPC lipid bilayer and the amphipathic helix 8 was oriented parallel to the plane of the membrane at approximately the lipid/water interface. The model membrane simulation cell was constructed with the replacement method, using scripts derived from CHARMM-GUI (33). The CHARMM22 protein force field with CMAP corrections (34, 35) and the CHARMM 36 lipid force field (36) were used in this study. Parameters for GDP were obtained by analogy to ADP using the nucleic acid force field (37), and those for *sn*-2-arachidonoylglycerol were derived from the lipid force field (17, 36). The lipidation sites are covalent modifications of their respective amino acids. The parameters for the palmitoylation sites were taken from our earlier simulations (17). Parameters for the myristoylation of $G\alpha_i$ and prenylation of the $G\gamma_2$ covalent linkages were taken by analogy with existing CHARMM force field parameters. Given that the primary role for these lipidation sites in these simulations is to anchor their respective proteins to the lipid matrix, no further optimization was performed. All lipidation parameters and patches used to generate the topologies are available upon request. Charge neutrality was enforced with addition of chloride counter ions, and an overall ionic strength of 0.1 M was obtained by adding NaCl. The final system contained 451 POPC lipid molecules, the protein complex, ions, and solvating water molecules with a simulation cell size of 130.0 × 130.0 × 170.6 Å.

Initial Minimization and Equilibration

To relieve poor initial contacts, 500 steps of steepest descent minimization were performed using CHARMM (38), with all heavy atoms of the protein complex fixed. This was followed by 20,000 steps of conjugate gradient minimization using NAMD (39). The fully minimized system was heated in 10 K increments to 310 K with restraints on the protein (force constant of 10 kcal/mol/Å^2/5.0 kcal/mol/Å^2 for the backbone/side chains and ligands respectively), on the POPC phosphates (force constant of 5.0 kcal/mol/Å^2), and a harmonic dihedral restraint on the POPC cis double bond and the glycerol c2 chiral center (force constant of 500 kcal/mol/rad^2). At each increment, 500 steps of minimization were performed followed by 20 ps of dynamics at the higher temperature. Equilibration was continued for 100 ps of molecular dynamics, and then the restraints were released in six steps over 1.5ns.

Details of Molecular Dynamics Simulations

For all production runs, NAMD (39) was used. Long range electrostatics were included using PME (40) with a 10-Å short range cutoff, and van der Waals interactions were treated with a switching function and a 10-Å cutoff. The NPT ensemble, as implemented in NAMD, was used to maintain temperature (T = 310 K, damping coefficient of 2 ps^{-1}) and pressure (p = 1.01325 bar, piston period/decay of 100/50 fs). High frequency bonds to hydrogen were restrained using the shake method implemented in NAMD allowing a 2-fs integration time step. Production dynamics was performed on a Blue Gene supercomputer (41) located at the Thomas J. Watson Research Center and on the BSBC cluster at University of North Carolina at Greensboro. Two separate trajectories were run for this complex. Results from these trajectories each at 1 μs in length are reported here. All analyses were performed using visual molecular dynamics (42) and LOOS (43).

Measuring the Angle of Rotation for $G\alpha_{i1}\beta_1\gamma_2$ Relative to the CB_2 Bundle

To measure the rotation of the G protein under the CB_2 receptor throughout the trajectories, the CB_2 receptor TMH bundle for each nanosecond of trajectory 1 and trajectory 2 was superimposed on the transmembrane region of the CB_2 receptor starting structure (t = 0 ns). The atoms used for the superposition were K1.32(33) to S1.59(60), P2.38(68) to N2.63(93), A3.23(104) to R3.55(136), R4.39(147) to M4.62(170), D5.38(189) to K5.64(215), L6.33(243) to A6.60(270), and K7.33(279) to R7.56(302). Two centers of mass were calculated as follows: 1) the center of mass of Gα Ras-like domain (GTPase domain) backbone atoms Glu-33 to Gly-60 and Thr-181 to Asp-328 (this excludes the C-terminal α5 helix and the N-terminal helix); and 2) the center of mass of the Gβ subunit, Asp-38 to Asn-340 (this excludes the N-terminal helix). The vector between these two centers of mass was calculated for the starting structure (t = 0 ns) and for each 1-ns frame of each

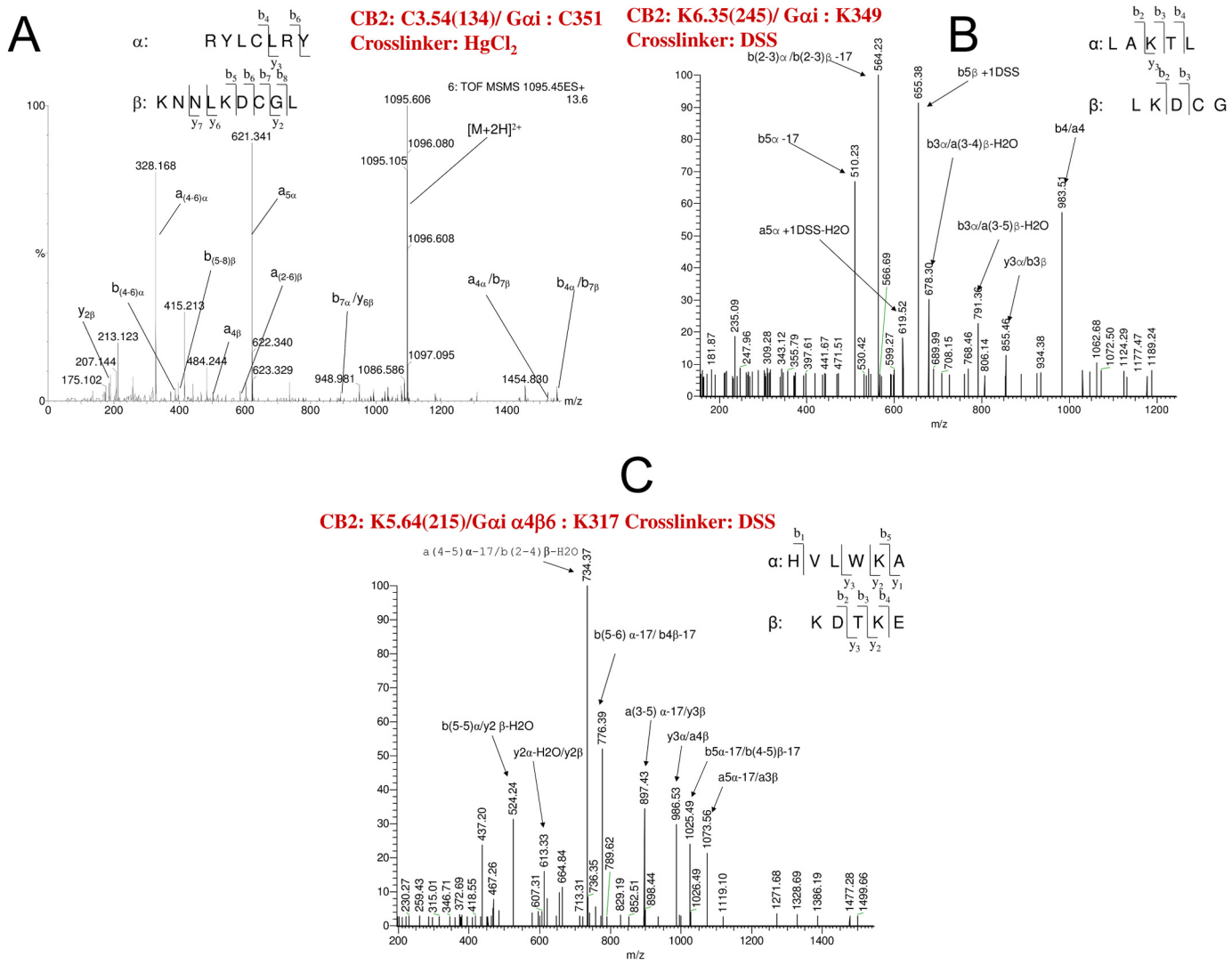

FIGURE 1. *A*, ESI-MS/MS spectrum of a cross-linked peptide between CB_2 and $G\alpha_i$ is presented here. The $[M + 2H]^{2+}$ peak at *m/z* 1095.105 (M = 2188.21) was selected as the precursor ion with a collision energy of 35 eV. The peptide α from CB_2 and the peptide β from $G\alpha_i$ cross-linked between Cys-134 and Cys-351. *B*, ESI-MS/MS spectrum of a cross-linked peptide between CB_2 and $G\alpha_i$ is presented here. The $[M + 2H]^{2+}$ peak at *m/z* 609.30 (M = 1216.60) was selected as the precursor ion with a collision energy of 35 eV. The peptide α from CB_2 and the peptide β from $G\alpha_i$ cross-linked between Lys-245 and Lys-349. *C*, ESI-MS/MS spectrum of a cross-linked peptide between CB_2 and $G\alpha_i$ is presented here. The $[M + 2H]^{2+}$ peak at *m/z* 755.89 (M = 2264.67) was selected as the precursor ion with a collision energy of 35 eV. The peptide α from CB_2 and the peptide β from $G\alpha_i$ cross-linked between Lys-215 and Lys-317.

trajectory. The angle between the starting structure vector and that of each trajectory time point was projected into the *x-y* plane and measured.

RESULTS

Mass Spectrometry Identification of CB_2 and $G\alpha_i$ Cross-links—To identify contacts between CB_2 and $G\alpha_i$, the CB_2 receptor and $G\alpha_i$ were cross-linked with either DSS (Lys-Lys) or $HgCl_2$ (Cys-Cys). Protein complexes were then purified by an M-2 anti-FLAG affinity column. Following SDS-PAGE separation, bands of the cross-linked CB_2·G_i complexes were excised and subjected to enzymatic digestion with pepsin. We used the non-specific enzyme pepsin to digest the cross-linked CB_2·G_i protein complex, because there are very few trypsin digestion sites in the CB_2 regions in which we were interested. The peptide mixtures resulting from in-gel digestions were analyzed by LC-MS/MS mass spectrometry. Data analysis was performed with the aid of the on-line server MS3D (24). The MS/MS spectrum of each candidate peptide was then manually checked to see whether it is a validated CB_2-G protein cross-linked peptide. Several important guidelines were used for identification of cross-linked peptide. 1) The main MS/MS peaks should match fragment ions. 2) Fragment ions from each of the two peptides that are cross-linked should be found. 3) Fragments that contain both peptides and linker should be found.

The ESI-MS/MS spectrum of cross-linked peptides between CB_2 and $G\alpha_i$ are shown in Fig. 1 (*A*–*C*). The fragment ions corresponding to two cross-linked peptides are designated with either the α (peptide from CB_2) or β (peptide from $G\alpha_i$) subscript to indicate the peptide of origin. In Fig. 1*A*, the spectrum can be assigned to two peptides: peptide α from CB_2 with a sequence of RYLCLRY and peptide β from $G\alpha_i$ with a sequence of KNNLKDCGL. The only cysteines in these two sequences that would have been available for cross-linking are Cys-134 in CB_2 and Cys-351 in $G\alpha_i$. Close inspection revealed the presence

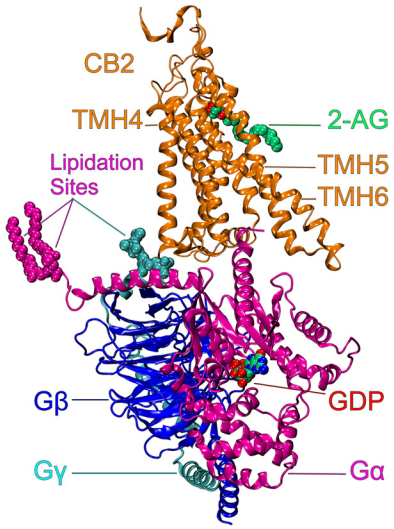

FIGURE 2. **Initial 2-AG/CB_2 R*·$G\alpha_{i1}\beta_1\gamma_2$ complex is presented here.** This dock was based on the crystal structure of the β2 adrenergic receptor in complex with $G\alpha_s$ protein (32). The CB_2 receptor is shown in *orange* bound to 2-AG (VdW *green carbons* and *red oxygens*). The $G\alpha_{i1}$ subunit of the $G\alpha_{i1}\beta_1\gamma_2$ heterotrimer is in *magenta*; $G\beta_1$ is in *blue,* and $G\gamma_2$ is in *cyan*. The palmitic and myristic acids attached to $G\alpha_{i1}$ are shown in VdW colored *magenta*. The geranylgeranyl group attached to $G\gamma_2$ is shown in VdW and colored *cyan*. GDP is bound between the helical and Ras-like domains of $G\alpha_{i1}$. Here, GDP is shown in VdW display with carbons, nitrogens, and oxygens colored *green, blue,* and *red,* respectively.

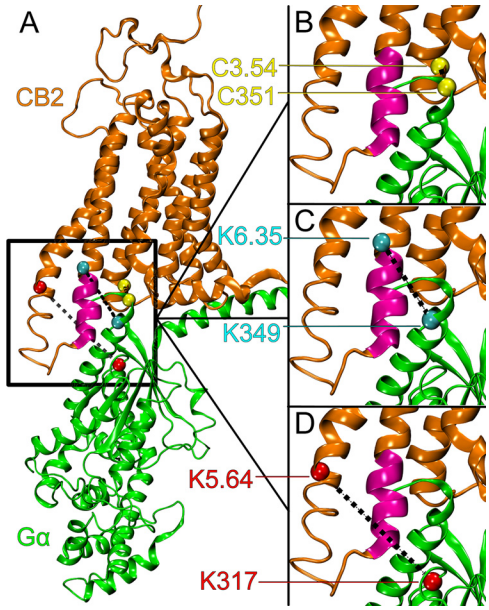

FIGURE 3. *A,* this figure shows the spatial location of the three cross-links identified between CB_2 R* and $G\alpha_{i1}$ protein in the starting structure for MD. *B,* Cα positions of the two residues linked using $HgCl_2$, C3.54(134) on CB_2 and Cys-351 on the $G\alpha_{i1}$ α-5 helix (i-3 residue) are shown here in *yellow*. *C,* Cα positions of two residues cross-linked with DSS, K6.35(245) on CB_2 TMH6 and Lys-349 on the $G\alpha_{i1}$ α5 helix (i-5 residue on C-terminal) are shown in *cyan*. *D,* Cα positions of another pair of residues cross-linked with DSS, K5.64(215) on CB_2 TMH5 and Lys-317 on the $G\alpha_{i1}$ α4β6 loop are colored *red*. The intracellular end of TMH6 that sterically obstructs this cross-link in the initial complex is colored *magenta*.

of three ions that originate from cleavage reactions involving both peptide chains, *i.e. b7*α/*y6*β, a4α/b7β, and *b4*α/*b7*β.

In Fig. 1*B*, the spectrum can be assigned to two peptides: peptide α from CB_2 with a sequence of LAKTL and peptide β from $G\alpha_i$ with a sequence of LKDCG. The only lysines in these two sequences that would have been available for cross-linking were Lys-245 in CB_2 and Lys-349 in $G\alpha_i$. The spectrum was closely examined for the possible presence of fragment ions originating from cleavages involving both peptide chains. There are five ions that originate from cleavage reactions involving both peptide chains. For example, y3α/b3β demonstrates clearly the cross-link between Lys-245 in CB_2 and Lys-349 in $G\alpha_i$.

In Fig. 1*C*, the spectrum can be assigned to two peptides as follows: peptide α from CB_2 with a sequence of HVLWKA and peptide β from $G\alpha_i$ with a sequence of KDTKE. There are eight ions that originate from cleavage reactions involving both peptide chains. Among these, y2α-H_2O/y2β demonstrates directly the cross-link between Lys-215 in CB_2 and Lys-317 in $G\alpha_i$.

Initial CB_2 R/$G\alpha_{i1}\beta_1\gamma_2$ Protein Dock*

Orientation of $G\alpha_{i1}\beta_1\gamma_2$ Protein—Our initial dock of CB_2 R* with $G\alpha_{i1}\beta_1\gamma_2$ protein (Fig. 2) was based on the crystal structure of the β2 adrenergic receptor in complex with the G_s protein (32). In this structure, the C-terminal α5 helix of $G\alpha_s$ is inserted between TMH3, TMH5, and TMH6, pointing toward the TMH7/Hx8 "elbow" region. TMH5 is packed closely with the C-terminal α5 helix. This orientation of $G\alpha_s$ places the N terminus of $G\alpha_s$ below TMH3 and TMH4, while the receptor IC2 loop fits in the region between the C and N termini of $G\alpha_s$.

Cysteine Cross-link between TMH3 and $G\alpha_{i1}$ C-terminal α5 Helix—The Cα-Cα distance range for formation of a cysteine cross-link using $HgCl_2$ is 7–10 Å (44, 45). The cysteine cross-link identified by LC-MS/MS analysis from the $HgCl_2$ (Cys-Cys) cross-linking study was found to be between C3.54(134) and Cys-351 on the $G\alpha_{i1}$ α5 helix (i-3 residue). The Cα-Cα distance between these two residues in the initial CB_2·$G\alpha_{i1}\beta_1\gamma_2$ complex was found to be 10.6 Å, which is just 0.6 Å outside the range for a cysteine cross-link formation using $HgCl_2$. The Cα positions of the cross-linked residues (*colored yellow*) at $t = 0$ ns in the context of the whole complex is shown in Fig. 3*A*. Fig. 3*B* presents a close-up view.

Lys-Lys Cross-links—The spacer arm length, N-N distance reported for DSS is 11.4 Å (46). L-Lysine measures 6.4 Å from the α carbon to nitrogen (47). This makes 24.2 Å the maximum Cα-Cα distance for formation of a Lys-Lys cross-link. The first lysine cross-link identified by LC-MS/MS analysis was between K6.35(245) on TMH6 and Lys-349 on the $G\alpha_{i1}$ α5 helix (i-5 residue on C-terminal). In the initial CB_2·$G\alpha_{i1}\beta_1\gamma_2$ complex, these residues were 17 Å apart (Cα-Cα), which is within the range for formation of the DSS (Lys-Lys) cross-link. In addition, the space between these two residues provided no steric obstruction to cross-link formation. The Cα position of the cross-linked residues (colored *cyan*) at $t = 0$ ns in the context of the whole complex is shown in Fig. 3*A*. Fig. 3*C* presents a close-up view.

The initial Cα-Cα distance for the second Lys-Lys cross-link between K5.34(215) on TMH5 and Lys-317 in the α4β6 region of $G\alpha_{i1}$ was 24.5 Å. This distance is only 0.3 Å outside the range for the formation of these Lys-Lys cross-links. However, it is not sterically possible to form this cross-link even if the distance was lower because the space between these two residues is blocked by the intracellular end of TMH6. This is illustrated in

Fig. 3*D*, where the intracellular extension of the TMH6 (shown in *magenta*) provides this steric obstruction ($t = 0$ ns). In Fig. 3*D*, the Cα positions of K5.64 and Lys-317 are colored *red*. This suggests that during the dynamic interaction of the two proteins, this region may change conformation allowing these residues to be cross-linked. Our MD simulations of the CB_2 R*·$G\alpha_{i1}\beta_1\gamma_2$ protein complex embedded in a POPC bilayer test this hypothesis. Fig. 4 illustrates the full system for trajectory 1 simulated over time, including the POPC bilayer (lipid acyl chains, *cyan*; phosphate atoms in phospholipid headgroup, *open gold circles*), the CB2 receptor (*orange*), and $G\alpha_{i1}\beta_1\gamma_2$ protein (*green*) with the $G\alpha_{i1}$ α5 helix shown in *yellow*.

Molecular Dynamics Simulations

MD calculations reported here used the results of cross-linking experiments to validate the receptor·G protein complex that emerged from our simulations. Cross-linking information was not used as a constraint for these simulations. It is also important to note that because of pepsin digestion, it is impossible to know whether all three cross-links occurred in a single CB_2·$G\alpha_i$ complex and whether each cross-link was found in a different CB_2·$G\alpha_i$ complex or any other permutation between these two extremes. In other words, we do not know in advance if all three distance constraints implied by the cross-linking are ever met simultaneously. In the starting structure for the MD simulations, the Cys-Cys cross-link is just outside the range for cross-link formation. One of the Lys-Lys cross-links is within range to form in the initial CB_2·G_i protein complex similar to β2-AR*·$G\alpha_s\beta_1\gamma_2$ complex. The second Lys-Lys cross-link, however, is not initially possible due to steric obstruction from the IC extension of TMH6.

Results from our two independent 1-μs long trajectories suggest that conformational changes occur in both CB_2 and $G\alpha_{i1}\beta_1\gamma_2$ during the first 300–400 ns of the trajectories, as these proteins optimize their interaction with each other; $G\alpha_{i1}\beta_1\gamma_2$, re-orients with respect to the receptor and uses a CB_2 IC-2 loop interaction to register the two proteins into new orientations, whereas TMH5 and TMH6 on CB_2 move outward, reorganizing the associated IC-3 loop. These changes are discussed in detail below.

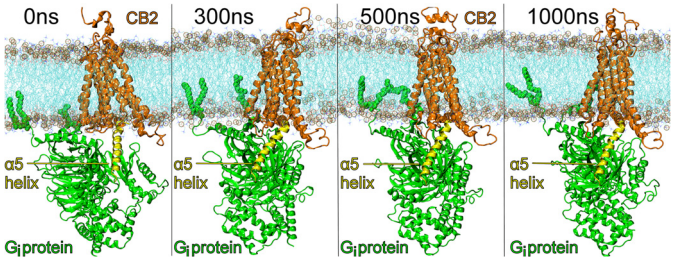

FIGURE 4. **This figure illustrates the full system for trajectory 1 simulated over time here, including the POPC bilayer (fatty acid acyl chains, *cyan*; phosphate atoms in phospholipid headgroup, *open gold circles*), the CB_2 receptor (*orange*), and $G\alpha_{i1}\beta_1\gamma_2$ protein (*green*) with the $G\alpha_{i1}$ α5 helix shown in *yellow*.**

$G\alpha_{i1}\beta_1\gamma_2$ Re-orientation relative to CB_2

Rotation of $G\alpha_{i1}\beta_1\gamma_2$—Fig. 5*A* illustrates the change about the *z* axis in $G\alpha_{i1}\beta_1\gamma_2$ orientation relative to CB_2 that occurs within the first 300 ns in trajectory 1. Here, the perspective is from the receptor interface toward the cytoplasm through the TMH bundle (the CB_2 receptor is omitted from the view for clarity). A clockwise rotation of ~25° can be clearly seen by considering the change in position of the N-terminal helix of $G\alpha_{i1}$ (Fig. 5*A*, shown in cylinder display: *purple cylinder* ($t = 0$ ns) *versus green cylinder* ($t = 300$ ns)). A similar rotation occurs in trajectory 2 within the first 400 ns (not shown). Fig. 5*B* shows the evolution of the rotation angle for trajectory 1 (*black*) and trajectory 2 (*blue*). The *red* and *yellow lines* in Fig. 5*B* represent the running averages. It is clear here that the distances plateau at about 300 ns for trajectory 1 and 400 ns for trajectory 2. Although the rotation angle for trajectory 1 stabilizes to ~25°, the rotation for trajectory 2 is ~35°.

Change in $G\alpha_{i1}$ C-terminal α5 Helix Tilt—Fig. 6 illustrates that another important change in $G\alpha_{i1}\beta_1\gamma_2$ orientation relative to CB_2 occurred during the MD runs. Here, the intracellular ends of TMH5-6-7 and Hx8 are shown with TMH-1-2-3-4

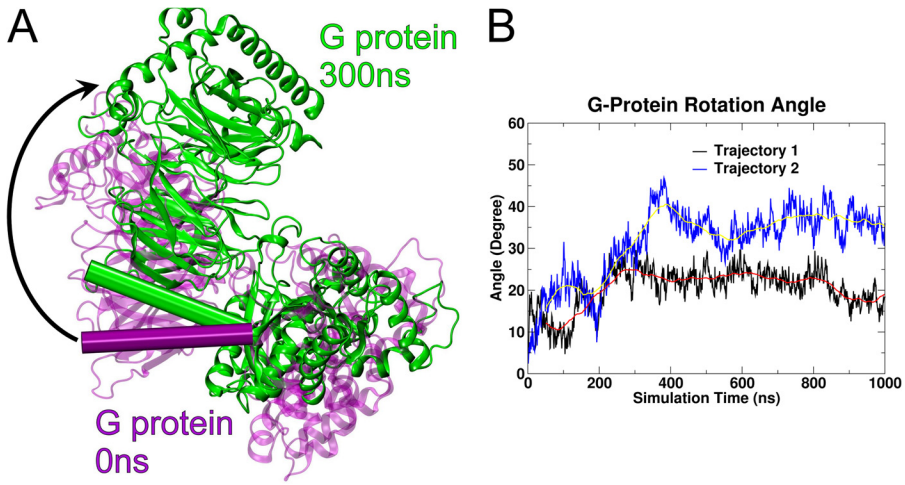

FIGURE 5. *A*, this figure illustrates for trajectory 1 that a rotation of the entire $G\alpha_{i1}\beta_1\gamma_2$ protein ($t = 0$ ns, *purple*; $t = 300$ ns, *green*) relative to CB_2 occurs along the *z* axis. Here the view is from the receptor interface toward the cytoplasm. The CB_2 TMH bundle has been turned off for clarity. A clockwise rotation of ~25° can be clearly seen by considering the change in position of the N-terminal helix of $G\alpha_{i1}$ (shown in *cylinder* display: *purple cylinder* ($t = 0$ ns) *versus green cylinder* ($t = 300$ ns). A similar clockwise rotation occurred in trajectory 2 (not shown). *B*, rotation angle for $G\alpha_{i1}\beta_1\gamma_2$ relative to the CB_2 TMH bundle over time in trajectory 1 (*black line*) and trajectory 2 (*blue line*) is illustrated here. The *red* and *yellow lines* represent the running average over 100 ns for trajectory 1 and 2, respectively.

omitted for clarity. The C-terminal α5 helix of $G\alpha_{i1}$ is shown in cylinder display (Fig. 6, *green*). In trajectory 1 (Fig. 6*A*), the C-terminal α5 helix of $G\alpha_{i1}$ changed from a tilt toward the TMH7-Hx8 elbow (as seen in the crystal structure of the β2-AR (32)) to a tilt more aligned with the membrane normal, bringing the extreme C terminus near the IC end of TMH6. This change occurred over the first 300 ns of the MD production run and was maintained through the rest of the trajectory ($t = 300$ ns → $t = 1000$ ns). Results were similar for trajectory 2 (Fig. 6*B*) except that the change in orientation happened over the first 400 ns. In both trajectories, the α5 helix changes its orientation by pivoting about a point near the center of the α5 helix in a rigid body motion. The helix also does not roll nor undergo a face shift.

IC-2-$G\alpha_{i1}\beta_1\gamma_2$ "Registering" Interaction

The rotation of $G\alpha_{i1}\beta_1\gamma_2$ about the *z* axis (illustrated in Fig. 5) promotes an interaction between the IC-2 loop of CB_2 and a hydrophobic pocket on $G\alpha_{i1}$ (see Fig. 7). This hydrophobic pocket is composed of residues immediately after the $G\alpha_{i1}$ N terminus (Val-34), residues on the $G\alpha_{i1}$ β1 and β2 sheets (Leu-194 and Phe-196), as well as residues on the $G\alpha_{i1}$ α5 helix (Ile-344, Ile-343, Thr-340, and Phe-336). In our initial CB_2 $R^*/G\alpha_{i1}\beta_1\gamma_2$ dock (based on the β2-AR/$G\alpha_s\beta_1\gamma_2$ crystal structure), the IC-2 loop of CB_2 was located between the N-terminal helix and C-terminal helix of $G\alpha_{i1}$, on top of the loop connecting the β2 and β3 sheets. Fig. 7 ($t = 0$ ns) illustrates the hydrophobic pocket and the orientation of the receptor IC-2 loop relative to this pocket at the beginning of each trajectory. As the result of the rotation of $G\alpha_{i1}\beta_1\gamma_2$ about the *z* axis discussed previously (see Fig. 5), an IC-2 loop residue, Pro-139, establishes a hydrophobic interaction with the hydrophobic pocket residues on $G\alpha_{i1}$ within the first 300 ns of the trajectory 1 (Fig. 7*A*) and 400 ns of trajectory 2 (Fig. 7*B*). Over both 1-μs trajectories, Pro-139 entered and exited the hydrophobic pocket several times, but the rotation of $G\alpha_{i1}\beta_1\gamma_2$ about the *y* axis ceased once this registering interaction was established around 300 ns for trajectory 1 and 400 ns for trajectory 2.

The interaction of Pro-139 with the hydrophobic pocket can also be followed by considering the solvent-accessible surface area of Pro-139 over the course of each trajectory or the interaction energy of Pro-139 with the hydrophobic pocket over the course of the trajectory. At the start of the trajectory 1, the solvent-accessible surface area of Pro-139 was 200 $Å^2$ ($t = 0$ ns), but it decreased to 80 $Å^2$ during the period between 250 and 300 ns (*black line* in Fig. 8*A*) and for trajectory 2, the solvent-accessible surface area of Pro-139 was 200 $Å^2$ ($t = 0$ ns), but decreased to 100 $Å^2$ during the period between 350 and 400 ns (*blue line* in Fig. 8*A*). The interaction energy between Pro-139 and the hydrophobic pocket was close to zero at the start of trajectory 1, but it dropped to −7 kcal/mol between 250 and 300 ns (*black line* Fig. 8*B*). For trajectory 2, the interaction energy dropped to −5 kcal/mol between 350 and 400 ns (*blue line,* Fig. 8*B*).

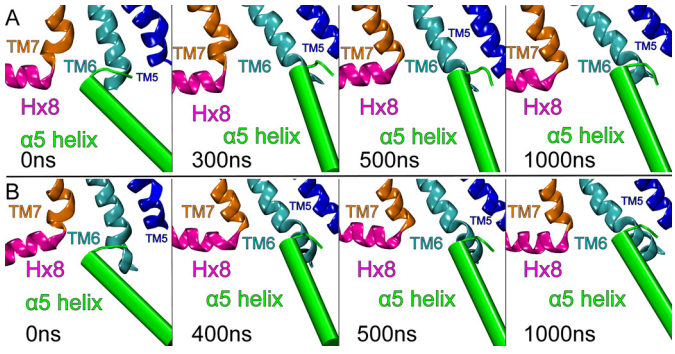

FIGURE 6. **Another important change in $G\alpha_{i1}\beta_1\gamma_2$ orientation relative to CB2 occurred during the MD runs.** Here, the intracellular ends of TMH5-6-7 and Hx8 are shown with TMH-1-2-3-4 omitted for clarity. The C-terminal α5 helix of $G\alpha_{i1}$ is shown in *cylinder* display (*green*). *A,* in trajectory 1, the C-terminal α5 helix of $G\alpha_{i1}$ changed from a tilt toward the TMH7-Hx8 elbow (as seen in the crystal structure of the β2-AR (32)) to a tilt more aligned with the membrane normal, bringing the extreme C terminus near the IC end of TMH6. This change occurred over the first 300 ns of the MD production run and was maintained throughout the rest of the trajectory ($t = 300$ ns → $t = 1000$ ns). *B,* results were similar for trajectory 2 except that the change in orientation happened over the first 400 ns.

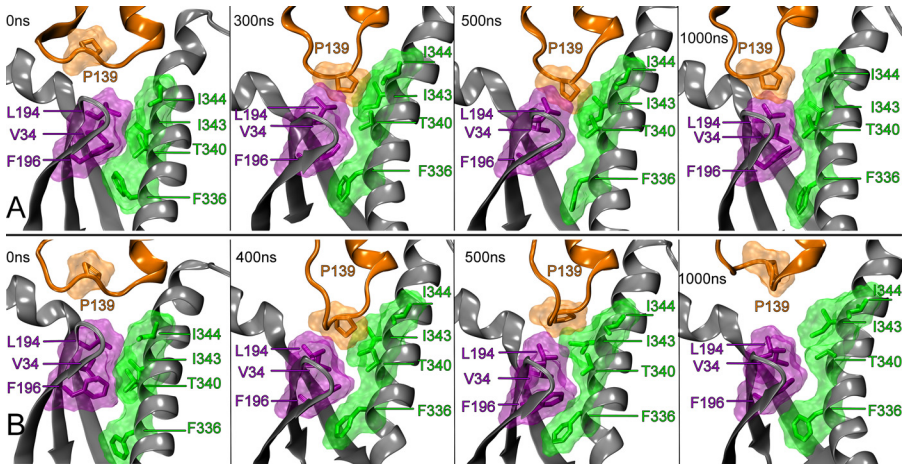

FIGURE 7. **IC-2/$G\alpha_{i1}\beta_1\gamma_2$ registering interaction.** The interaction between the CB_2 IC-2 loop residue (Pro-139, colored *orange*) and a hydrophobic pocket on $G\alpha_{i1}$ is shown here. This hydrophobic pocket is composed of residue(s) immediately after the $G\alpha_{i1}$ N terminus (Val-34, colored *purple*), residue(s) on the $G\alpha_{i1}$ β1, and β2 sheets (Leu-194 and Phe-196, colored *purple*), as well as residues on the $G\alpha_{i1}$ α5 helix (Phe-336, Thr-340, Ile-343, and Ile-344, colored *green*). *A,* this shows the interaction of Pro-139 with the hydrophobic pocket at selected time points over 1 μs in trajectory 1. The first interaction of Pro-139 with the hydrophobic pocket occurred at $t = 300$ ns. *B,* Pro-139 interaction with the hydrophobic pocket at selected time points over 1 μs in trajectory 2 is shown here. The first interaction with the hydrophobic pocket in trajectory 2 occurred at $t = 400$ ns.

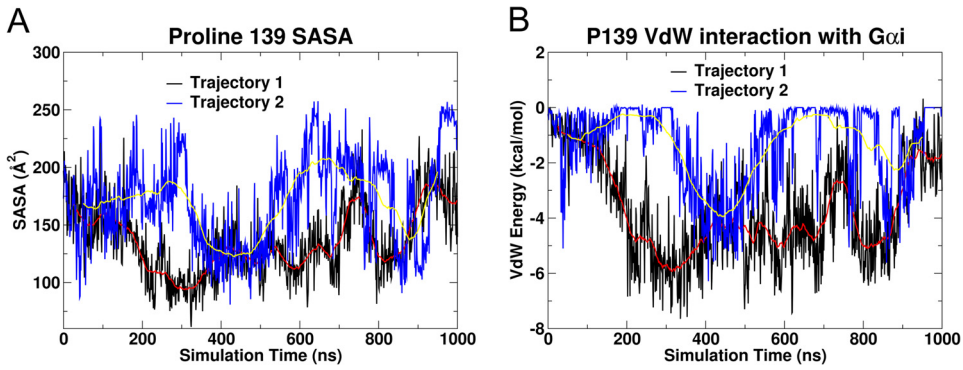

FIGURE 8. **These plots (trajectory 1, *black*; trajectory 2, *blue*) show the change in the solvent-accessible surface area (*A*) and van der Waals interaction energy for the Pro-139 (CB_2 IC-2 loop) interaction with the $G\alpha_{i1}$ hydrophobic pocket (*B*).** The *red* and *yellow lines* represent the running average over 100 ns for trajectory 1 and trajectory 2, respectively. Over the 1000-ns trajectory, Pro-139 entered and exited the hydrophobic pocket several times, but the rotation of $G\alpha_{i1}\beta_1\gamma_2$ about the *z* axis ceased once this anchoring interaction was first established at 300 ns for trajectory 1 and 400 ns for trajectory 2 (see Fig. 7 for further detail).

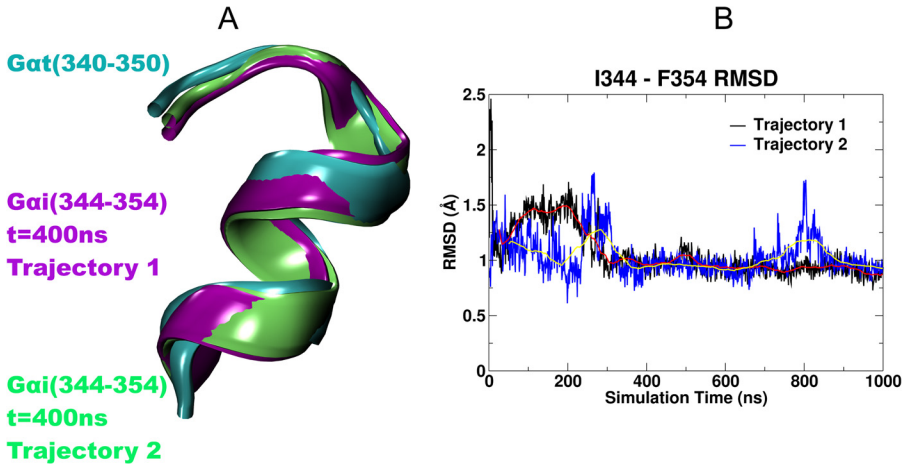

FIGURE 9. *A*, this figure shows a comparison of the $G\alpha_t$ (residues 340–350) NMR structure (27) (*cyan*) with the corresponding last 10 residues of $G\alpha_{i1}$ at $t = 400$ ns in trajectory 1 (*purple*) and trajectory 2 (*green*). It is clear that the two segments from both the trajectories have very similar shapes. *B*, we calculated the r.m.s.d. of the α carbons of the last 10 residues of $G\alpha_{i1}$ in our simulation *versus* the NMR structure. The r.m.s.d. plot *versus* simulation time shows that this region of the C terminus of $G\alpha_{i1}$ undergoes changes during the period $t = 0$ ns $\rightarrow t = 300$ ns for trajectory 1 (*black line*) and $t = 0$ ns $\rightarrow t = 40$ ns for trajectory 2 (*blue line*) when the tilt of the $G\alpha_{i1}$ α5 helix is changing, but the r.m.s.d. reaches a stable value by 300 ns for trajectory 1 and 400 ns for trajectory 2 and remains low thereafter. The *red* and *yellow lines* represent the running average over 100 ns for trajectory 1 and 2, respectively.

Shape of α5 Helix C-terminal Portion

The crystal structure of $G\alpha_{i1}\beta_1\gamma_2$ is missing the last 10 residues of the $G\alpha_{i1}$ α5 helix. The three-dimensional structure of the transducin (G_t) α subunit C-terminal undecapeptide $G\alpha_t$ ^{340}IKENLKDCGLF^{350} was determined by Kisselev *et al.* (27) using transferred nuclear Overhauser effect spectroscopy, while it was bound to photoexcited rhodopsin (Protein Data Bank 1AQG). Light activation of rhodopsin caused a dramatic shift from a disordered conformation of $G\alpha_t$ (340–350) to a binding motif with a helical turn followed by an open reverse turn centered at Gly-348, with a helix-terminating C capping motif of an αL type. We used this NMR structure to complete the missing C terminus of $G\alpha_{i1}$ in our initial model of the CB_2 G protein complex. Fig. 9*A* shows a comparison of the $G\alpha_t$ (340–350) NMR structure (*cyan*) with the corresponding last 10 residues of $G\alpha_{i1}$ at $t = 400$ ns in each simulation (trajectory 1, *purple*; trajectory 2, *green*). It is clear that in both the trajectories, the two segments have very similar shapes. We calculated the r.m.s.d. of the Cα's of the last 10 residues of $G\alpha_{i1}$ in our simulations *versus* the NMR structure. The r.m.s.d. plot in Fig. 9*B* shows that this region of the C terminus of $G\alpha_{i1}$ undergoes changes during the period ($t = 0$ ns $\rightarrow t = 300$ ns) for trajectory 1 and ($t = 0$ ns $\rightarrow t = 400$ ns) for trajectory 2 when the tilt of the $G\alpha_{i1}$ α5 helix is changing, but the r.m.s.d. reaches a stable value by 300 ns for trajectory 1 and 400 ns for trajectory 2 and remains low thereafter.

Why Does the α5 Helix Change Its Tilt?

There are two differences between the CB_2·$G\alpha_{i1}\beta_1\gamma_2$ and β2-AR·$G\alpha_s\beta_1\gamma_2$ complexes that may contribute to the change in tilt of the α5 helix. These are Gα sequence differences and GPCR sequence differences.

Sequence Differences, α5 Helix—The reorientation of the $G\alpha_{i1}$ α5 helix illustrated in Fig. 5 may be attributable in part to sequence differences between $G\alpha_s$ and $G\alpha_i$. The sequences of the last 10 residues of the various isoforms of Gα ($G\alpha_{i1}$, $G\alpha_{i2}$, $G\alpha_o$, $G\alpha_t$, $G\alpha_s$, $G\alpha_q$, etc.) have high homology; however, there is an important difference at the i-4 position. For the $G\alpha_i$ proteins, this position is occupied by a negatively charged residue (Asp in $G\alpha_{i1}$ and $G\alpha_{i2}$; Glu in $G\alpha_{i3}$). For $G\alpha_s$, however, this position is an uncharged residue (Gln-390(i-4)). Fig. 10 illustrates the difference in the interaction of the extreme C terminus of $G\alpha_{i1}$ with the receptor that occurs partly as a consequence of this sequence difference. In the β2-AR (see Fig. 10*A*), R3.50 has an

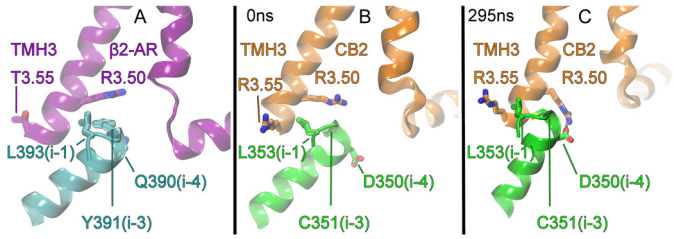

FIGURE 10. **This figure illustrates the interaction between receptor residues at the intracellular end of TMH3 with the three (i-1, i-3 and i-4) residues of the C-terminal α5 helix of $G\alpha_{i1}$.** *A,* this figure shows that R3.50 of the β2-AR receptor interacts with Tyr-391(i-3) on $G\alpha_s$ (32). *B,* this figure shows that in the initial $CB_2{\cdot}G\alpha_{i1}\beta_1\gamma_2$ complex, R3.50 interacts with Cys-351(i-3) on $G\alpha_{i1}$ and R3.55 interacts with Leu-353(i-1). Here, the tilt of the α5 helix is very similar to that of $G\alpha_s$ in *A*. *C,* however, after 295 ns in trajectory 1, the tilt angle of the $G\alpha_{i1}$ α5 helix has changed permitting CB_2 R3.50 to form a salt bridge with Asp-350(i-4) on $G\alpha_{i1}$, whereas the hydrocarbon portion of R3.55 has a VdW interaction with Leu-353(i-1). Note here that to establish these interactions, the α5 helix changes its tilt angle to be more aligned with the membrane normal.

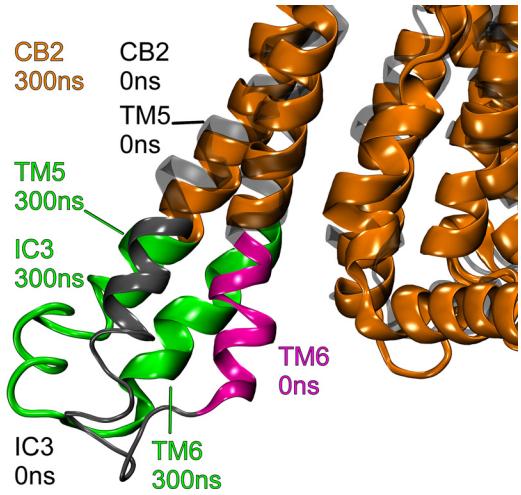

FIGURE 11. **To accommodate the re-orientation of the $G\alpha_{i1}$ α5 helix and the rotation of $G\alpha_{i1}\beta_1\gamma_2$, CB_2 undergoes an outward movement of TMH5-TMH6 and the associated IC-3 loop moves away from the CB_2 TMH bundle.** This is illustrated in Fig. 11 for trajectory 1 from the TMH4-5 perspective. The CB_2 structure at $t = 0$ ns is colored *gray* here, and the CB_2 structure at $t = 300$ ns is colored *orange*.

aromatic stacking interaction with Tyr-391(i-3) on the $G\alpha_s$ α5 helix. Although our initial dock of $G\alpha_i$ with CB_2 R* mimicked this (see Fig. 10*B*), during the initial 300–400 ns of the trajectories, the α5 helix changed its tilt angle to be more aligned with the membrane normal. This tilt change allows CB_2 R3.50 to now interact with Asp-350(i-4) on the $G\alpha_i$ α5 helix (see Fig. 10*C*), whereas CB_2 R3.55 interacts with Leu-353(i-1) on the $G\alpha_i$ α5 helix. This latter interaction is a van der Waals interaction.

Sequence Differences, TMH5-TMH6 Movement—To accommodate the re-orientation of the $G\alpha_{i1}$ α5 helix and the rotation of $G\alpha_{i1}\beta_1\gamma_2$, CB_2 undergoes an outward movement of TMH5-TMH6, and the associated IC-3 loop moves away from the CB_2 TMH bundle. This is illustrated in Fig. 11 for trajectory 1. This is facilitated by the fact that both TMH5 and TMH6 have hinge points that allow these helices to move away from the TMH bundle when CB_2 is activated (17). TMH5 hinges at G5.53(204), whereas the hinge point for TMH6 is at G6.38(248). Fig. 12 shows that the position of the CB_2 IC-3 loop relative to the $G\alpha_{i1}$ $\alpha4\beta6$ loop changes before 300 ns in trajectory 1. Here, the G protein has clearly undergone a rotation that places the $\alpha4\beta6$ loop of $G\alpha_{i1}$ near the IC-3 loop of CB_2. This movement also removes the steric obstruction to the formation of the Lys-Lys cross-link between K5.34(215) on TMH5 and Lys-317 in the $\alpha4\beta6$ region of $G\alpha_{i1}$ that existed at the outset of the simulation (see Fig. 3*D*). Similar results were obtained with trajectory 2.

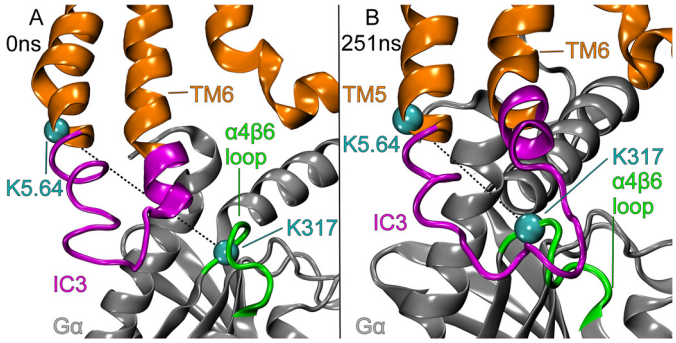

FIGURE 12. **This figure shows that the position of the CB_2 IC-3 loop relative to the $G\alpha_{i1}$ $\alpha4\beta6$ loop changes before 300 ns in trajectory 1.** Here, the G protein has clearly undergone a rotation that places the $\alpha4\beta6$ loop of $G\alpha_{i1}$ near the IC-3 loop of CB_2. This movement also removes the steric obstruction to the formation of the Lys-Lys cross-link between K5.34(215) on TMH5 and Lys-317 in the $\alpha4\beta6$ region of $G\alpha_{i1}$ that existed at the outset of the simulation (see Fig. 3*D*). Similar results were obtained with trajectory 2.

Cross-link Correlations

Cysteine Cross-link between TMH3 and C-terminal $G\alpha_{i1}$ α5 Helix—To test whether experimentally obtained cross-links were possible in trajectories 1 and 2, we considered Cα-Cα distances for each pair of linked residues. We compared these distances to the range of Cα-Cα distances over which the cross-linking has been shown to form. In some trajectories, this distance was below the cutoff distance for the entire trajectory. In others, there were only regions of the trajectory that were below the cutoff. We begin here by discussing each of the cross-links individually. At the end of this section, we assess in what percentage of the trajectories is the Cα-Cα distance below the cutoff at the same time. Fig. 13*A* shows a plot of the Cα-Cα distance between C3.54(134) on CB_2 and Cys-351 on the $G\alpha_{i1}$ α5 helix (i-3 residue on C-terminal) for both trajectories. This plot has the distance range for cysteine cross-link formation indicated by the *green lines* in Fig. 13. This distance was 10.6 Å in the starting structure, which was just 0.6 Å outside the cross-link range. The distance does decrease into the range of 7–10 Å, for multiple times in both trajectories. As a result, we conclude that our MD simulations suggest that the formation of a Cys-Cys cross-link is possible.

Cross-link between TMH6 and C-terminal α5 Helix of $G\alpha_{i1}$—Fig. 13*B* shows a plot of the Cα-Cα distance for the Lys-Lys cross-link between K6.35(245) on CB_2 and Lys-349 on the $G\alpha_{i1}$ α5 helix (i-5 residue on C-terminal) for both the trajectories. The *green line* in Fig. 13*B* at 24.2 Å indicates the distance below which a cross-link would be possible. The plot shows that this distance remained around 15 Å during the entire 1-μs MD simulation for both the trajectories. In addition, there were no steric obstructions of this interaction present at any time in either trajectory. Therefore, we conclude that our MD simulations suggest that the formation of this Lys-Lys cross-link is possible.

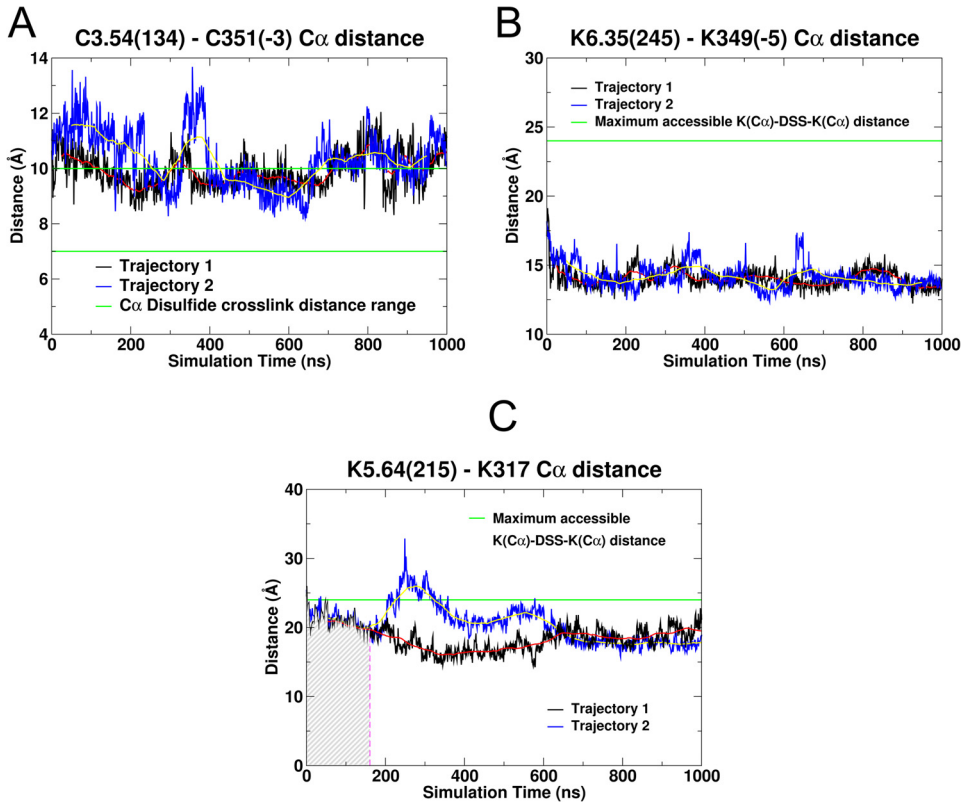

FIGURE 13. **Plot of Cα-Cα distance as a function of simulation time is shown here for the three cross-links reported here.** Trajectory 1 is shown in *black,* and trajectory 2 is in *blue*. The *red* and *yellow lines* represent the running average over 100 ns for trajectory 1 and trajectory 2 respectively. *A,* Cα-Cα distance between C3.54(134) and Cys-351 on the $G\alpha_{i1}$ α5 helix (i-3 residue on C-terminal) is shown here. The *green lines* at 7 and 10 Å correspond to the distance range for cross-link formation between two cysteines using $HgCl_2$. *B,* Cα-Cα distance between K6.35(245) and Lys-349 on the $G\alpha_{i1}$ α5 helix (i-5 residue on C-terminal) is shown here. The *green lines* at 24.2 Å are the maximum Cα distance to form a cross-link formation between two lysines using DSS. *C,* Cα-Cα distance between K5.64(215) and Lys-317 on the $G\alpha_{i1}$ α4β6 loop is shown here. The *green lines* at 24.2 Å are the maximum Cα distance to form a cross-link formation between two lysines using DSS. The *hatched area* before 200 ns represents that part of trajectory during for which the intracellular end of TMH6 sterically obstructs this cross-link. This corresponds to the section of TMH6 colored *magenta* in Fig. 3*D*.

Cross-link between TMH5 and the $G\alpha_{i1}$ α4β6 Loop—We have indicated above that one consequence of the $G\alpha_{i1}\beta_1\gamma_2$ rotation relative to CB_2 is that TMH5-IC3-TMH6 moves away from the TMH bundle at the IC side in the first 300 ns for trajectory 1 and 400 ns for trajectory 2. Prior to this movement, it is structurally impossible to cross-link K5.34(215) on TMH5 and Lys-317 in the α4β6 region of $G\alpha_{i1}$ even though the Cα-Cα distance between these residues is below the 24.2Å cutoff for cross-link formation. Fig. 13*C* shows a plot of the Cα-Cα distance for this Lys-Lys cross-link for both trajectories. That section of the simulation for which the cross-link is structurally not possible is indicated by the *hashed region* in Fig. 13*C*. For trajectory 1 (Fig. 13*C, black line*), once the structural interference is removed as TMH5-IC3-TMH6 moves away from the bundle, the cross-link is possible at all other time points. Trajectory 2 (Fig. 13*C, blue line*) does have one region that goes above the allowed distance after the steric obstruction is cleared (200–375 ns). After this region, the Cα-Cα distance for trajectory 2 remains below the cutoff. Therefore, our MD simulations suggest that the formation of this Lys-Lys cross-link is also possible.

Finally, we assessed at 1-ns intervals for both trajectories, those times for which all three sets of Cα-Cα distances were below the cutoff (and therefore possible) at the same time. We found that in trajectory 1, this percentage was 60.8%, although for trajectory 2, this percentage was 33.4%.

DISCUSSION

High resolution x-ray structures have been obtained for multiple class A ("rhodopsin-like") GPCRs (3–6, 48–56), various G protein heterotrimers (Gαβγ) (26, 57, 58), and isolated Gα subunits in different functional states (59–61). Combined with biochemical and biophysical data, these structures reveal a surface on Gα that is predicted to face the intracellular side of GPCRs. Information about the nature of this interface has been obtained via x-ray crystallography and chemical cross-linking studies. At present, there is only one crystal structure of a GPCR·protein complex available (32), which shows the interaction of β2-AR with the G_s protein after GDP has dissociated from the Gα subunit. This structure represents an empty state that exists between the GDP-bound and GTP-bound G protein, artificially stabilized by a nanobody, insertion of which was necessary for crystallization (32).

Chemical cross-linking studies of protein-protein interactions can identify pairs of residues that come close enough to each other to form a respective cross-link. The identification of multiple cross-link sites can provide information about the relative orientation of the two interacting proteins.

In this paper, a comprehensive GPCR-$G\alpha_i$ protein chemical cross-linking strategy was applied with the goal of ascertaining the orientation of the CB_2 receptor relative to $G\alpha_{i1}$. These experiments revealed three cross-links as follows: 1) a cysteine cross-link between TMH3 residue C3.54(134) and Cys-351 on the $G\alpha_{i1}$ α5 helix (i-3 residue); 2) a lysine cross-link between TMH6 residue K6.35(245) and Lys-349 on the $G\alpha_{i1}$ α5 helix (i-5 residue); and 3) a lysine cross-link between TMH5 residue K5.64(215) and Lys-317 on the $G\alpha_{i1}$ α4β6 loop. An examination of the initial complex we constructed to a mimic the β2-AR*·$G\alpha_s\beta_1\gamma_2$ x-ray crystal structure (32) revealed that one of these cross-links (K6.35(245) to Lys-349) is possible in the initial complex. A second cross-link (C3.54(134) to Cys-351) is only 0.6 Å above the Cα-Cα distance limit for cross-linking in the initial complex. But the third cross-link was sterically impossible in the initial complex. This suggested that either the orientation of the G protein with respect to a GPCR varies depending on the receptor and G protein to be complexed or that the orientation of $G\alpha_s\beta_1\gamma_2$ with respect to the β2-AR* in the crystal structure changes after GDP leaves the $G\alpha_s$ subunit, as has occurred in the β2-AR*·$G\alpha_s\beta_1\gamma_2$ crystal structure.

To understand the origins of the experimental cross-links between CB_2 and $G\alpha_i$ identified in this paper, we undertook microsecond time scale molecular dynamic simulations of the CB_2 R*·$G\alpha_{i1}\beta_1\gamma_2$ complex in a POPC bilayer. We show here that when two MD runs of the CB_2 R*·$G\alpha_{i1}\beta_1\gamma_2$ complex in lipid are initiated using the same G protein orientation (including the angle of the $G\alpha_{i1}$ α5 helix) as seen in the β2-AR*/$G\alpha_s\beta_1\gamma_2$ crystal structure, rearrangements ensue fairly quickly in each. There is a gross clockwise rotation of the entire G protein underneath CB_2 R* during the first 300 ns (trajectory 1) or 400 ns (trajectory 2) of the production runs. This rotation ceases once an interaction is established between the IC-2 loop residue, Pro-139 and a hydrophobic pocket on $G\alpha_{i1}$ formed by residues Val-34, Leu-194, Phe-196, Phe-336, Thr-340, Ile-343, and Ile-344.

A change in the tilt of the $G\alpha_{i1}$ α5 helix also occurs early in the trajectories facilitated by the outward movement of TMH6 and TMH5 at their IC ends. The change in tilt allows R3.50 on CB_2 to form a salt bridge with Asp-350(i-4) on the $G\alpha_{i1}$ α5 helix.

Importance of the $G\alpha_{i1}\alpha$5 Helix and the Change in Its Tilt Angle—In this cross-linking study, a cysteine cross-link was formed between TMH3 residue C3.54(134) and Cys-351 on the $G\alpha_{i1}$ α5 helix (i-3 residue). The extreme C terminus was one of the first regions within Gα identified as being critical to receptor-promoted activation. Hamm *et al.* (62) first demonstrated that synthetic peptides corresponding to the C terminus of $G\alpha_t$ could block rhodopsin-promoted activation, suggesting that the C terminus of Gα is a critical receptor-binding site. Alanine-scanning experiments confirmed that the C terminus/α5 helix was essential for the rhodopsin-promoted activation of $G\alpha_t$ (63). In many early G protein crystal structures, the extreme C terminus of Gα was unresolved. The first three-dimensional structure of the transducin (G_t) α subunit C-terminal undecapeptide $G\alpha_t$ ^{340}IKENLKDCGLF^{350} bound to photoexcited rhodopsin registered in the Protein Data Bank was determined by using transferred nuclear Overhauser effect spectroscopy (27). Light activation of rhodopsin caused a dramatic shift from a disordered conformation of $G\alpha_t$ (340–350) to a binding motif with a helical turn followed by an open reverse turn centered at Gly-348, with a helix-terminating C capping motif of an α L type. Docking of the NMR structure to the GDP-bound x-ray structure of G_t reveals that photoexcited rhodopsin promotes the formation of a continuous helix over residues 325–346 terminated by the C-terminal helical cap with a unique cluster of crucial hydrophobic side chains. Subsequently, this C-terminal region has been resolved in three GPCR crystal structures as follows: 1) the bovine opsin*·Gα·C-terminal peptide complex (64); 2) meta II rhodopsin in complex with an 11-amino acid C-terminal fragment derived from Gα (two residues mutated) (65); and 3) the β2-AR*·$G\alpha_s\beta_1\gamma_2$ complex (32). In each of these structures, the shape of the extreme C terminus is quite similar to the original NMR structure. In this work, this NMR structure was used to complete the $G\alpha_{i1}$ structure that was docked in CB_2 R*. The r.m.s.d. plot in Fig. 9*B* shows that the shape of the last 10 residues in the C-terminal region has a low r.m.s.d. after the first 300 ns of production simulation for trajectory 1 and 400 ns for trajectory 2 when compared with the NMR structure.

We also report here that the insertion angle of the $G\alpha_{i1}$ α5 helix changed from its starting angle (which mimicked the β2-AR*·$G\alpha_s\beta_1\gamma_2$ complex (32)). Two reasons for this change are the position of the IC end of TMH5 in CB_2 R* and a key sequence difference between $G\alpha_i$ and $G\alpha_s$ at the i-3 position on the $G\alpha_i$ α5 helix. One striking difference between the β2-AR and CB_2 sequences is that the β2-AR has the highly conserved P5.50, whereas CB_2 lacks this proline in TMH5 (L5.50 in CB_2). In the β2-AR*·$G\alpha_s\beta_1\gamma_2$ complex (32), TMH6 has moved away from the TMH bundle and broken the ionic lock (R3.50/E6.30), thus exemplifying an activated GPCR. The proline kink region of TMH5 flexes but moves TMH5 toward the TMH bundle interior. When the α5 helix of $G\alpha_s$ inserts in this activated structure, it must insert in an opening formed by TMH6's outward movement. This region extends over to the elbow region of TMH7-Hx8. In the case of CB_2, the C-terminal α5 helix of $G\alpha_{i1}$ can insert into a wider opening, one formed by the TMH5 and TMH6 outward movement. This in turn allows the angle of insertion to change in CB_2.

R3.50 has been shown to be crucial for CB_2 signal transduction. Feng and Song (66) reported no stimulation of agonist-induced [^{35}S]GTPγS binding for the R3.50A mutant in CB_2. We show here that the change in the tilt angle of the α5 helix also permits formation of a salt bridge between R3.50 on CB_2 and Asp-350(i-4) on the $G\alpha_i$ α5 helix. Asp-350(i-4) occupies a position in the C terminus of $G\alpha_i$ that has an important divergence from $G\alpha_s$. For the $G\alpha_i$, this position is occupied by a negatively charged residue (Asp in $G\alpha_{i1}$ and $G\alpha_{i2}$; Glu in $G\alpha_{i3}$). For $G\alpha_s$, however, this position is an uncharged residue (Gln-390(i-4)). Fig. 10 illustrates the difference in the interaction of the extreme C terminus of $G\alpha_{i1}$ with the receptor that occurs partly as a consequence of this sequence difference. In the β2-AR (see Fig. 10*A*), R3.50 has an aromatic stacking interaction with Tyr-391(i-3) on the $G\alpha_s$ α5 helix. Although our initial dock of $G\alpha_i$ with CB2 R* mimicked this (see Fig. 10*B*), after 295 ns in trajectory 1, the tilt of the α5 helix has changed such that $G\alpha_{i1}$ moves

toward TMH5-TMH6, allowing R3.50 to now interact with Asp-350(i-4) (see Fig. 10*C*), although the hydrophobic part of R3.55 interacts with Leu-353(i-1). A similar change occurred in trajectory 2.

Second Intracellular Loop Interaction with Gα Protein—Interactions between GPCR IC-2 loops and G protein have been shown to be critical in GPCR/G protein coupling for numerous receptors. The IC-2 loop of the muscarinic M3 receptor has been shown to interact with the N-terminal region of $G\alpha_q$ protein (67). IC-2 interactions also have been shown to be critical for coupling in the follicle-stimulating hormone receptor (FSH) with $G\alpha_s$ (68). In the β2-AR*/$G\alpha_s\beta_1\gamma_2$ crystal structure, IC-2 loop residue, Phe-139, inserts into an aromatic/hydrophobic pocket on $G\alpha_s$ composed of His-41, Val-217, Phe-129, Phe-376, Arg-380, and Ile-383 on the $G\alpha_s$ C-terminal region and $G\alpha_s$, β2, and β3 sheets (see Fig. 4*c* in Ref. 32). The importance of this interaction is underscored by mutagenesis studies that demonstrate that a β2-AR F139A mutation significantly impairs β2-AR coupling to $G\alpha_s$ (69). We show here that $G\alpha_{i1}\beta_1\gamma_2$ rotation about the *z* axis ceased once the IC-2 loop residue, Pro-139, establishes a hydrophobic interaction with the hydrophobic pocket residues on $G\alpha_{i1}$ (Figs. 6 and 7). The two proteins appear to be in register once this interaction occurs. Consistent with this idea, no further $G\alpha_{i1}\beta_1\gamma_2$ rotation occurs in either trajectory. In support of the importance of this interaction, Zheng *et al.* (70) have reported that a P139A mutation in CB_2 results in the loss of coupling with $G\alpha_i$.

Third Intracellular Loop Interaction with the $\alpha_4\beta_6$ Region of Gα—Our chemical cross-linking strategy led to a DSS (Lys-Lys) cross-link between the TMH5 residue K5.64(215) and Lys-317 on the $G\alpha_{i1}$ α4β6 loop. In the MD simulations reported here, this cross-link becomes possible only after $G\alpha_{i1}\beta_1\gamma_2$ rotation under CB_2 (see Figs. 4, 5, 11, and 12). The importance of α4/β6 loop residues to the GPCR·G protein complex formation has been shown for multiple GPCRs. Slessareva *et al.* (71) have shown that the $G\alpha_{i1}$ α4 helix-α4/β6 loop are involved in 5-HT1a, 5-HT1b, and muscarinic M2 receptor interactions. For the rhodopsin·transducin ($G\alpha_t$) complex, residues in the $G\alpha_t$ $\alpha_4\beta_6$ loop (Arg-310 to Lys-313) were shown to cross-link with residues in the IC-3 loop of rhodopsin using a photoactivatable reagent, *N*-[(2-pyridyldithio)ethyl],4-azidosalicylamide (72). For the rat M3 muscarinic acetylcholine receptor (M3R)·$G\alpha_q$ complex system, a cross-link has been reported between a D321C mutation on $\alpha_4\beta_6$ loop of $G\alpha_q$ and a K7.58(548)C mutation on M3R. Here the cross-linking agent was a short bi-functional, irreversible chemical cross-linker bismaleimisoethane (67).

Conclusions—The result of this study is a CB_2 R*·$G\alpha_{i1}\beta_1\gamma_2$ complex in which the proteins are in the correct register as indicated by chemical cross-linking studies. The next stage of this project will be the study of the changes that complex formation with CB_2 R* induces in $G\alpha_{i1}\beta_1\gamma_2$. Our ultimate goal will be the activated state of $G\alpha_{i1}\beta_1\gamma_2$ in which GDP has been released.

Acknowledgment—We acknowledge the many helpful discussions with Dr. Klaus Gawrisch on this project.

REFERENCES

1. Pierce, K. L., Premont, R. T., and Lefkowitz, R. J. (2002) Seven-transmembrane receptors. *Nat. Rev. Mol. Cell Biol.* **3,** 639–650
2. Regard, J. B., Sato, I. T., and Coughlin, S. R. (2008) Anatomical profiling of G protein-coupled receptor expression. *Cell* **135,** 561–571
3. Hanson, M. A., Roth, C. B., Jo, E., Griffith, M. T., Scott, F. L., Reinhart, G., Desale, H., Clemons, B., Cahalan, S. M., Schuerer, S. C., Sanna, M. G., Han, G. W., Kuhn, P., Rosen, H., and Stevens, R. C. (2012) Crystal structure of a lipid G protein-coupled receptor. *Science* **335,** 851–855
4. Wu, H., Wacker, D., Mileni, M., Katritch, V., Han, G. W., Vardy, E., Liu, W., Thompson, A. A., Huang, X. P., Carroll, F. I., Mascarella, S. W., Westkaemper, R. B., Mosier, P. D., Roth, B. L., Cherezov, V., and Stevens, R. C. (2012) Structure of the human κ-opioid receptor in complex with JDTic. *Nature* **485,** 327–332
5. Manglik, A., Kruse, A. C., Kobilka, T. S., Thian, F. S., Mathiesen, J. M., Sunahara, R. K., Pardo, L., Weis, W. I., Kobilka, B. K., and Granier, S. (2012) Crystal structure of the micro-opioid receptor bound to a morphinan antagonist. *Nature* **485,** 321–326
6. Wang, C., Jiang, Y., Ma, J., Wu, H., Wacker, D., Katritch, V., Han, G. W., Liu, W., Huang, X. P., Vardy, E., McCorvy, J. D., Gao, X., Zhou, X. E., Melcher, K., Zhang, C., Bai, F., Yang, H., Yang, L., Jiang, H., Roth, B. L., Cherezov, V., Stevens, R. C., and Xu, H. E. (2013) Structural basis for molecular recognition at serotonin receptors. *Science* **340,** 610–614
7. Lefkowitz, R. J., and Shenoy, S. K. (2005) Transduction of receptor signals by β-arrestins. *Science* **308,** 512–517
8. Weis, W. I., and Kobilka, B. K. (2008) Structural insights into G-protein-coupled receptor activation. *Curr. Opin. Struct. Biol.* **18,** 734–740
9. Clapham, D. E., and Neer, E. J. (1997) G protein βγ subunits. *Annu. Rev. Pharmacol. Toxicol.* **37,** 167–203
10. Smrcka, A. V. (2008) G protein βγ subunits: central mediators of G protein-coupled receptor signaling. *Cell. Mol. Life Sci.* **65,** 2191–2214
11. Lin, Y., and Smrcka, A. V. (2011) Understanding molecular recognition by G protein βγ subunits on the path to pharmacological targeting. *Mol. Pharmacol.* **80,** 551–557
12. Hamm, H. E. (1998) The many faces of G protein signaling. *J. Biol. Chem.* **273,** 669–672
13. Galiègue, S., Mary, S., Marchand, J., Dussossoy, D., Carrière, D., Carayon, P., Bouaboula, M., Shire, D., Le Fur, G., and Casellas, P. (1995) Expression of central and peripheral cannabinoid receptors in human immune tissues and leukocyte subpopulations. *Eur. J. Biochem.* **232,** 54–61
14. Storr, M., Gaffal, E., Saur, D., Schusdziarra, V., and Allescher, H. D. (2002) Effect of cannabinoids on neural transmission in rat gastric fundus. *Can. J. Physiol. Pharmacol.* **80,** 67–76
15. Wright, K. L., Duncan, M., and Sharkey, K. A. (2008) Cannabinoid CB2 receptors in the gastrointestinal tract: a regulatory system in states of inflammation. *Br. J. Pharmacol.* **153,** 263–270
16. Racz, I., Nadal, X., Alferink, J., Baños, J. E., Rehnelt, J., Martín, M., Pintado, B., Gutierrez-Adan, A., Sanguino, E., Manzanares, J., Zimmer, A., and Maldonado, R. (2008) Crucial role of CB(2) cannabinoid receptor in the regulation of central immune responses during neuropathic pain. *J. Neurosci.* **28,** 12125–12135
17. Hurst, D. P., Grossfield, A., Lynch, D. L., Feller, S., Romo, T. D., Gawrisch, K., Pitman, M. C., and Reggio, P. H. (2010) A lipid pathway for ligand binding is necessary for a cannabinoid G protein-coupled receptor. *J. Biol. Chem.* **285,** 17954–17964
18. Demuth, D. G., and Molleman, A. (2006) Cannabinoid signalling. *Life Sci.* **78,** 549–563
19. Bouaboula, M., Desnoyer, N., Carayon, P., Combes, T., and Casellas, P. (1999) Gi protein modulation induced by a selective inverse agonist for the peripheral cannabinoid receptor CB2: implication for intracellular signalization cross-regulation. *Mol. Pharmacol.* **55,** 473–480
20. Bouaboula, M., Poinot-Chazel, C., Marchand, J., Canat, X., Bourrié, B., Rinaldi-Carmona, M., Calandra, B., Le Fur, G., and Casellas, P. (1996) Signaling pathway associated with stimulation of CB2 peripheral cannabinoid receptor. Involvement of both mitogen-activated protein kinase and induction of Krox-24 expression. *Eur. J. Biochem.* **237,** 704–711
21. Preininger, A. M., Meiler, J., and Hamm, H. E. (2013) Conformational

flexibility and structural dynamics in GPCR-mediated G protein activation: a perspective. *J. Mol. Biol.* **425,** 2288–2298
22. Zhang, R., Kim, T. K., Qiao, Z. H., Cai, J., Pierce, W. M., Jr., and Song, Z. H. (2007) Biochemical and mass spectrometric characterization of the human CB2 cannabinoid receptor expressed in *Pichia pastoris*–importance of correct processing of the N terminus. *Protein Expr. Purif.* **55,** 225–235
23. Jensen, O. N., Wilm, M., Shevchenko, A., and Mann, M. (1999) Sample preparation methods for mass spectrometric peptide mapping directly from 2-DE gels. *Methods Mol. Biol.* **112,** 513–530
24. Yu, E. T., Hawkins, A., Kuntz, I. D., Rahn, L. A., Rothfuss, A., Sale, K., Young, M. M., Yang, C. L., Pancerella, C. M., and Fabris, D. (2008) The collaboratory for MS3D: a new cyberinfrastructure for the structural elucidation of biological macromolecules and their assemblies using mass spectrometry-based approaches. *J. Proteome Res.* **7,** 4848–4857
25. Schilling, B., Row, R. H., Gibson, B. W., Guo, X., and Young, M. M. (2003) MS2Assign, automated assignment and nomenclature of tandem mass spectra of chemically cross-linked peptides. *J. Am. Soc. Mass Spectrom.* **14,** 834–850
26. Wall, M. A., Coleman, D. E., Lee, E., Iñiguez-Lluhi, J. A., Posner, B. A., Gilman, A. G., and Sprang, S. R. (1995) The structure of the G protein heterotrimer Giα1β1γ2. *Cell* **83,** 1047–1058
27. Kisselev, O. G., Kao, J., Ponder, J. W., Fann, Y. C., Gautam, N., and Marshall, G. R. (1998) Light-activated rhodopsin induces structural binding motif in G protein α subunit. *Proc. Natl. Acad. Sci. U.S.A.* **95,** 4270–4275
28. Kisselev, O. G., and Downs, M. A. (2003) Rhodopsin controls a conformational switch on the transducin γ subunit. *Structure* **11,** 367–373
29. Parenti, M., Viganó, M. A., Newman, C. M., Milligan, G., and Magee, A. I. (1993) A novel N-terminal motif for palmitoylation of G-protein α subunits. *Biochem. J.* **291,** 349–353
30. Preininger, A. M., Van Eps, N., Yu, N. J., Medkova, M., Hubbell, W. L., and Hamm, H. E. (2003) The myristoylated amino terminus of Gα(i)(1) plays a critical role in the structure and function of Gα(i)(1) subunits in solution. *Biochemistry* **42,** 7931–7941
31. Sanford, J., Codina, J., and Birnbaumer, L. (1991) γ-Subunits of G proteins, but not their α- or β-subunits, are polyisoprenylated. Studies on post-translational modifications using in vitro translation with rabbit reticulocyte lysates. *J. Biol. Chem.* **266,** 9570–9579
32. Rasmussen, S. G., DeVree, B. T., Zou, Y., Kruse, A. C., Chung, K. Y., Kobilka, T. S., Thian, F. S., Chae, P. S., Pardon, E., Calinski, D., Mathiesen, J. M., Shah, S. T., Lyons, J. A., Caffrey, M., Gellman, S. H., Steyaert, J., Skiniotis, G., Weis, W. I., Sunahara, R. K., and Kobilka, B. K. (2011) Crystal structure of the β2 adrenergic receptor-Gs protein complex. *Nature* **477,** 549–555
33. Jo, S., Kim, T., Iyer, V. G., and Im, W. (2008) CHARMM-GUI: a web-based graphical user interface for CHARMM. *J. Comput. Chem.* **29,** 1859–1865
34. MacKerell, A. D., Jr., Bashford, D., Bellott, M., Dunbrack, R. L., Jr., Evanseck, J. D., Field, M. J., Fischer, S., Gao, J., Guo, H., Ha, S., Joseph-McCarthy, D., Kuchnir, L., Kuczera, K., Lau, F. T. K., Mattos, C., Michnick, S., Ngo, T., Nguyen, D. T., Prodhom, B., Reiher, W. E., 3rd, Roux, B., Schlenkrich, M., Smith, J. C., Stote, R., Straub, J., Watanabe, M., Wiorkiewicz-Kuczera, J., Yin, D., and Karplus, M. (1998) All-atom empirical potential for molecular modeling and dynamics studies of proteins. *J. Phys. Chem. B* **102,** 3586–3616
35. Mackerell, A. D., Jr., Feig, M., and Brooks, C. L., 3rd (2004) Extending the treatment of backbone energetics in protein force fields: limitations of gas-phase quantum mechanics in reproducing protein conformational distributions in molecular dynamics simulations. *J. Comput. Chem.* **25,** 1400–1415
36. Klauda, J. B., Venable, R. M., Freites, J. A., O'Connor, J. W., Tobias, D. J., Mondragon-Ramirez, C., Vorobyov, I., MacKerell, A. D., Jr., and Pastor, R. W. (2010) Update of the CHARMM all-atom additive force field for lipids: validation on six lipid types. *J. Phys. Chem. B* **114,** 7830–7843
37. Foloppe, N., and MacKerell, A. D., Jr. (2000) All-atom empirical force field for nucleic acids: I. Parameter optimization based on small molecule and condensed phase macromolecular target data. *J. Comput. Chem.* **21,** 86–104
38. Brooks, B. R., Brooks, C. L., 3rd, Mackerell, A. D., Jr., Nilsson, L., Petrella, R. J., Roux, B., Won, Y., Archontis, G., Bartels, C., Boresch, S., Caflisch, A., Caves, L., Cui, Q., Dinner, A. R., Feig, M., Fischer, S., Gao, J., Hodoscek, M., Im, W., Kuczera, K., Lazaridis, T., Ma, J., Ovchinnikov, V., Paci, E., Pastor, R. W., Post, C. B., Pu, J. Z., Schaefer, M., Tidor, B., Venable, R. M., Woodcock, H. L., Wu, X., Yang, W., York, D. M., and Karplus, M. (2009) CHARMM: the biomolecular simulation program. *J. Comput. Chem.* **30,** 1545–1614
39. Phillips, J. C., Braun, R., Wang, W., Gumbart, J., Tajkhorshid, E., Villa, E., Chipot, C., Skeel, R. D., Kalé, L., and Schulten, K. (2005) Scalable molecular dynamics with NAMD. *J. Comput. Chem.* **26,** 1781–1802
40. Essmann, U., Perera, L., Berkowitz, M. L., Darden, T. A., Lee, J., and Pedersen, L. G. (1995) A smooth particle mesh Ewald method. *J. Chem. Phys.* **103,** 8577–8593
41. Gara, A., Blumrich, M. A., Chen, D., Chiu, G. L., Coteus, P., Giampapa, M. E., Haring, R. A., Heidelberger, P., Hoenicke, D., Kopcsay, G. V., Liebsch, T. A., Ohmacht, M., Steinmacher-Burow, B. D., Takken, T., and Vranas, P. (2005) Overview of the blue gene/L system architecture. *IBM J. Res. Dev.* **49,** 195–212
42. Humphrey, W., Dalke, A., and Schulten, K. (1996) VMD: visual molecular dynamics. *J. Mol. Graph.* **14,** 33–38
43. Romo, T. D., and Grossfield, A. (2009) LOOS: An Extensible Platform for Structural Analysis of Simulations. in *31st Annual International Conference of the IEEE EMBS*, *Minneapolis, September 2–6, 2009*, pp. 2332–2335, Springer-Verlag, Minneapolis, MN
44. Soskine, M., Steiner-Mordoch, S., and Schuldiner, S. (2002) Cross-linking of membrane-embedded cysteines reveals contact points in the EmrE oligomer. *Proc. Natl. Acad. Sci. U.S.A.* **99,** 12043–12048
45. Fass, D. (2012) Disulfide bonding in protein biophysics. *Annu. Rev. Biophys.* **41,** 63–79
46. Green, N. S., Reisler, E., and Houk, K. N. (2001) Quantitative evaluation of the lengths of homobifunctional protein cross-linking reagents used as molecular rulers. *Protein Sci.* **10,** 1293–1304
47. Banks, J. L., Beard, H. S., Cao, Y., Cho, A. E., Damm, W., Farid, R., Felts, A. K., Halgren, T. A., Mainz, D. T., Maple, J. R., Murphy, R., Philipp, D. M., Repasky, M. P., Zhang, L. Y., Berne, B. J., Friesner, R. A., Gallicchio, E., and Levy, R. M. (2005) Integrated modeling program, applied chemical theory (IMPACT). *J. Comput. Chem.* **26,** 1752–1780
48. Palczewski, K., Kumasaka, T., Hori, T., Behnke, C. A., Motoshima, H., Fox, B. A., Le Trong, I., Teller, D. C., Okada, T., Stenkamp, R. E., Yamamoto, M., and Miyano, M. (2000) Crystal structure of rhodopsin: A G protein-coupled receptor. *Science* **289,** 739–745
49. Rasmussen, S. G., Choi, H. J., Rosenbaum, D. M., Kobilka, T. S., Thian, F. S., Edwards, P. C., Burghammer, M., Ratnala, V. R., Sanishvili, R., Fischetti, R. F., Schertler, G. F., Weis, W. I., and Kobilka, B. K. (2007) Crystal structure of the human β2 adrenergic G-protein-coupled receptor. *Nature* **450,** 383–387
50. Jaakola, V. P., Griffith, M. T., Hanson, M. A., Cherezov, V., Chien, E. Y., Lane, J. R., Ijzerman, A. P., and Stevens, R. C. (2008) The 2.6 angstrom crystal structure of a human A2A adenosine receptor bound to an antagonist. *Science* **322,** 1211–1217
51. Warne, T., Serrano-Vega, M. J., Baker, J. G., Moukhametzianov, R., Edwards, P. C., Henderson, R., Leslie, A. G., Tate, C. G., and Schertler, G. F. (2008) Structure of a β1-adrenergic G-protein-coupled receptor. *Nature* **454,** 486–491
52. Wu, B., Chien, E. Y., Mol, C. D., Fenalti, G., Liu, W., Katritch, V., Abagyan, R., Brooun, A., Wells, P., Bi, F. C., Hamel, D. J., Kuhn, P., Handel, T. M., Cherezov, V., and Stevens, R. C. (2010) Structures of the CXCR4 chemokine GPCR with small-molecule and cyclic peptide antagonists. *Science* **330,** 1066–1071
53. Haga, K., Kruse, A. C., Asada, H., Yurugi-Kobayashi, T., Shiroishi, M., Zhang, C., Weis, W. I., Okada, T., Kobilka, B. K., Haga, T., and Kobayashi, T. (2012) Structure of the human M2 muscarinic acetylcholine receptor bound to an antagonist. *Nature* **482,** 547–551
54. Granier, S., Manglik, A., Kruse, A. C., Kobilka, T. S., Thian, F. S., Weis, W. I., and Kobilka, B. K. (2012) Structure of the δ-opioid receptor bound to naltrindole. *Nature* **485,** 400–404
55. Kruse, A. C., Hu, J., Pan, A. C., Arlow, D. H., Rosenbaum, D. M., Rosemond, E., Green, H. F., Liu, T., Chae, P. S., Dror, R. O., Shaw, D. E., Weis, W. I., Wess, J., and Kobilka, B. K. (2012) Structure and dynamics of the M3

muscarinic acetylcholine receptor. *Nature* **482,** 552–556
56. White, J. F., Noinaj, N., Shibata, Y., Love, J., Kloss, B., Xu, F., Gvozdenovic-Jeremic, J., Shah, P., Shiloach, J., Tate, C. G., and Grisshammer, R. (2012) Structure of the agonist-bound neurotensin receptor. *Nature* **490,** 508–513
57. Lambright, D. G., Sondek, J., Bohm, A., Skiba, N. P., Hamm, H. E., and Sigler, P. B. (1996) The 2.0 A crystal structure of a heterotrimeric G protein. *Nature* **379,** 311–319
58. Nishimura, A., Kitano, K., Takasaki, J., Taniguchi, M., Mizuno, N., Tago, K., Hakoshima, T., and Itoh, H. (2010) Structural basis for the specific inhibition of heterotrimeric Gq protein by a small molecule. *Proc. Natl. Acad. Sci. U.S.A.* **107,** 13666–13671
59. Coleman, D. E., and Sprang, S. R. (1998) Crystal structures of the G protein Giα1 complexed with GDP and Mg^{2+}: a crystallographic titration experiment. *Biochemistry* **37,** 14376–14385
60. Tesmer, J. J., Sunahara, R. K., Gilman, A. G., and Sprang, S. R. (1997) Crystal structure of the catalytic domains of adenylyl cyclase in a complex with Gsα.GTPγS. *Science* **278,** 1907–1916
61. Lambright, D. G., Noel, J. P., Hamm, H. E., and Sigler, P. B. (1994) Structural determinants for activation of the α-subunit of a heterotrimeric G protein. *Nature* **369,** 621–628
62. Hamm, H. E., Deretic, D., Arendt, A., Hargrave, P. A., Koenig, B., and Hofmann, K. P. (1988) Site of G protein binding to rhodopsin mapped with synthetic peptides from the α subunit. *Science* **241,** 832–835
63. Onrust, R., Herzmark, P., Chi, P., Garcia, P. D., Lichtarge, O., Kingsley, C., and Bourne, H. R. (1997) Receptor and $\beta\gamma$ binding sites in the α subunit of the retinal G protein transducin. *Science* **275,** 381–384
64. Scheerer, P., Park, J. H., Hildebrand, P. W., Kim, Y. J., Krauss, N., Choe, H. W., Hofmann, K. P., and Ernst, O. P. (2008) Crystal structure of opsin in its G-protein-interacting conformation. *Nature* **455,** 497–502
65. Choe, H. W., Kim, Y. J., Park, J. H., Morizumi, T., Pai, E. F., Krauss, N., Hofmann, K. P., Scheerer, P., and Ernst, O. P. (2011) Crystal structure of metarhodopsin II. *Nature* **471,** 651–655
66. Feng, W., and Song, Z. H. (2003) Effects of D3.49A, R3.50A, and A6.34E mutations on ligand binding and activation of the cannabinoid-2 (CB2) receptor. *Biochem. Pharmacol.* **65,** 1077–1085
67. Hu, J., Wang, Y., Zhang, X., Lloyd, J. R., Li, J. H., Karpiak, J., Costanzi, S., and Wess, J. (2010) Structural basis of G protein-coupled receptor-G protein interactions. *Nat. Chem. Biol.* **6,** 541–548
68. Ulloa-Aguirre, A., Uribe, A., Zariñán, T., Bustos-Jaimes, I., Pérez-Solis, M. A., and Dias, J. A. (2007) Role of the intracellular domains of the human FSH receptor in G(αS) protein coupling and receptor expression. *Mol. Cell. Endocrinol.* **260,** 153–162
69. Moro, O., Lameh, J., Högger, P., and Sadée, W. (1993) Hydrophobic amino acid in the i2 loop plays a key role in receptor-G protein coupling. *J. Biol. Chem.* **268,** 22273–22276
70. Zheng, C., Chen, L., Chen, X., He, X., Yang, J., Shi, Y., and Zhou, N. (2013) The second intracellular loop of the human cannabinoid CB2 receptor governs G protein coupling in coordination with the carboxyl-terminal domain. *PloS one* **8,** e63262
71. Slessareva, J. E., Ma, H., Depree, K. M., Flood, L. A., Bae, H., Cabrera-Vera, T. M., Hamm, H. E., and Graber, S. G. (2003) Closely related G-protein-coupled receptors use multiple and distinct domains on G-protein α-subunits for selective coupling. *J. Biol. Chem.* **278,** 50530–50536
72. Cai, K., Itoh, Y., and Khorana, H. G. (2001) Mapping of contact sites in complex formation between transducin and light-activated rhodopsin by covalent cross-linking: use of a photoactivatable reagent. *Proc. Natl. Acad. Sci. U.S.A.* **98,** 4877–4882